Atmos. Chem. Phys., 9, 2805–2824, 2009
www.atmos-chem-phys.net/9/2805/2009/

Atmospheric Chemistry and Physics

Studies of heterogeneous freezing by three different desert dust samples

P. J. Connolly[1], **O. Möhler**[2], **P. R. Field**[3], **H. Saathoff**[2], **R. Burgess**[1], **T. Choularton**[1], **and M. Gallagher**[1]

[1]School of Earth, Atmospheric and Environmental Sciences, The University of Manchester, UK
[2]IMK-AAF Forschungszentrum Karlsruhe, Germany
[3]Met Office, Exeter, UK

Received: 13 October 2008 – Published in Atmos. Chem. Phys. Discuss.: 8 January 2009
Revised: 7 April 2009 – Accepted: 7 April 2009 – Published: 27 April 2009

Abstract. We present results of experiments at the aerosol interactions and dynamics in the atmosphere (AIDA) chamber facility looking at the freezing of water by three different types of mineral particles at temperatures between −12°C and −33°C. The three different dusts are Asia Dust-1 (AD1), Sahara Dust-2 (SD2) and Arizona test Dust (ATD). The dust samples used had particle concentrations of sizes that were log-normally distributed with mode diameters between 0.3 and 0.5 µm and standard deviations, σ_g, of 1.6–1.9. The results from the freezing experiments are consistent with the singular hypothesis of ice nucleation. The dusts showed different nucleation abilities, with ATD showing a rather sharp increase in ice-active surface site density at temperatures less than −24°C. AD1 was the next most efficient freezing nuclei and showed a more gradual increase in activity than the ATD sample. SD2 was the least active freezing nuclei.

We used data taken with particle counting probes to derive the ice-active surface site density forming on the dust as a function of temperature for each of the three samples and polynomial curves are fitted to this data. The curve fits are then used independently within a bin microphysical model to simulate the ice formation rates from the experiments in order to test the validity of parameterising the data with smooth curves. Good agreement is found between the measurements and the model for AD1 and SD2; however, the curve for ATD does not yield results that agree well with the observations. The reason for this is that more experiments between −20 and −24°C are needed to quantify the rather sharp increase in ice-active surface site density on ATD in this temperature regime. The curves presented can be used as parameterisations in atmospheric cloud models where cooling rates of approximately 1°C min^{-1} or more are present to predict the concentration of ice crystals forming by the condensation-freezing mode of ice nucleation. Finally a polynomial is fitted to all three samples together in order to have a parameterisation describing the average ice-active surface site density vs. temperature for an equal mixture of the three dust samples.

1 Introduction

Recently Ansmann et al. (2008) presented lidar observations demonstrating that altocumulus (Ac) and layer clouds influenced by desert dust over the African continent, close to the source, seldom show any signs of glaciation for temperatures warmer than −20°C. This is apparently contradictory to the numerous observations by other authors in cumulus (Cu) clouds (see Hobbs and Rangno, 1985, 1990, for example). Another interesting finding was that in this temperature regime ($-30°C<T<0°C$), liquid drops were apparently required before the formation of ice. The measurements of Ansmann et al. therefore suggest that the freezing modes of ice nucleation, i.e. condensation-freezing/immersion freezing and not deposition are important ice formation mechanisms in layer clouds.

A further perplexing piece in the puzzle of atmospheric dust as ice nuclei (IN) comes from measurements made during the Cirrus Regional Study of Tropical Anvils and Cirrus Layers-Florida Area Cirrus Experiment CRYSTAL-FACE project, which demonstrated a possible link between the concentration of desert dust that advected across the Atlantic Ocean and the glaciation of layer clouds near the Florida

---

Correspondence to: P. J. Connolly
(p.connolly@man.ac.uk)

coast (DeMott et al., 2003; Sassen et al., 2003). In the case reported by Sassen et al. desert dust particles were inferred to glaciate a cloud at temperatures from −5.2 to −8.8°C.

Numerous laboratory observations have shown that when a sample of liquid drops that contain IN are subject to a fast cooling they freeze at a rate that is approximately proportional to the cooling rate. They also show that if this cooling is stopped the rate at which the drops freeze is much slower than when the drops are being cooled. To explain these observations Vali (1994) presented the time-dependent freezing rate (TDFR) theory for heterogeneous drop freezing. TDFR theory allows one to calculate the drop freezing rate of a sample in which there is a distribution of different IN contained within the drops; each different type of IN having a different temperature-dependent ice nucleation rate.

From TDFR theory two approximations can be made: (1) each sample unit (drop) is the same (i.e. the IN the drops contain all have the same ice nucleation rate). Under this approximation, known as the "stochastic hypothesis", the freezing of individual drops can be viewed as a Poisson distributed variable with respect to time and a nucleation rate equation can be applied to explain this, similar to that for radioactive decay. (2) The nucleation rates of the spectrum of the different IN contained in the drops are not smooth functions, but sharp transitions with respect to temperature; so sharp that the nucleation rate for one type of nucleus can be represented by a step function – i.e. ice-nucleation happens at a fixed temperature on a given type of nucleus. In this case the freezing rate can be described from the distribution of freezing temperatures of the nuclei within the drops – i.e. "the nucleus content" in the drops – $K(T)$ (ice germs $\mathrm{m}^{-3}\,{}^{\circ}\mathrm{C}^{-1}$) and the cooling rate, $\dot{T}$.

Drop freezing experiments were also conducted by Vali (1994) who studied the freezing rate of water containing suspended foreign material due to heterogeneous nucleation. He found that for water drops cooled at rates of the order of $-1^{\circ}\mathrm{C\,min}^{-1}$, the "nucleus content" (distribution of freezing temperatures in the nuclei) of the drops predicts the freezing rate well – i.e. the singular hypothesis holds. However, for samples with fixed temperatures, the stochastic, time dependent nature, although small, becomes non-negligible.

This conclusion is also supported by the more recent work of Vali (2007), who investigated the freezing temperatures of drops of water containing IN from two soil samples. Vali 's experiments had the drops placed on a cold stage and, during several cycles, he repeatedly lowered the temperature until they froze and then increased the temperature until they melted. He found evidence supporting a modified singular hypothesis. The finding that the temperature at which drop containing IN froze changed by very little upon repeated cycles led Vali to conclude that a modified singular hypothesis is appropriate.

Marcolli et al. (2007) looked at the freezing spectrum of drops containing so called ATD and analysed their results by comparing with three assumptions that were based on the classical nucleation theory. In classical nucleation theory ice germs are assumed to be spherical caps in contact with the nucleating material (i.e. the dust). The three assumptions were: (1) that each particle of ATD had the same contact angle (stochastic hypothesis); (2) that the contact angle varied between particles (singular hypothesis-a); and (3) that there was a distribution of active sites with different contact angles on each particle (singular hypthesis-b). Their basic finding was that the singular hypothesis best describes their results. However, neither of the approaches could reproduce the measurements in their entirety, which highlights the inadequacies of the classical approach.

Möhler et al. (2006) were motivated by the potential importance of dust as atmospheric IN; they studied and described heterogeneous deposition nucleation for cirrus (Ci) temperatures in the AIDA laboratory by the same three dust samples used in this paper – so called AD1; ATD and SD2. They found that to within their instrumental error, this "deposition" nucleation mode acted only while the supersaturation with respect to ice was increasing, and there was little explicit time dependence on the ice particle formation rate. This ice nucleation behaviour is consistent with the dust samples having a distribution of supersaturations at which they become active as IN – i.e. it is consistent with the singular nucleation hypothesis.

Since the study by Möhler et al., Zimmermann et al. (2008) investigated efficiency as IN of numerous minerals at different temperatures using an Environmental Scanning Electron Microscope (ESEM) to quantify the onset relative humidity of ice nucleation. They showed that in some cases the nucleation efficiency may also be a function of temperature.

Here we present further results from three campaigns at the AIDA facility to attempt to quantify ice nucleation behaviour on the three different types of dust particles in the temperature range $T > 235$ K. We also present the ice crystal habits, that were observed with the CPI during the experiments, mainly as supporting measurements, but also to look into any effects that nucleation may have on resulting ice crystal habit (e.g. Bailey and Hallett, 2002).

Section 2 describes the experiments; Sect. 3 gives an outline of the methods of data analysis we are using; Sect. 4 is the results and 5 and 6 are discussion and conclusion sections.

2 Experiments

2.1 Laboratory experiments and data collection

In order to investigate heterogeneous freezing we conducted experiments at the large AIDA cloud chamber. Cloud formation and evolution were simulated in the laboratory at the AIDA (see Fig. 1 for a schematic of the AIDA); the experiments aimed to form clouds under natural and controlled

Table 1. Log-normal fits to the PSD measured with a SMPS. The total particle number, N_L was generally variable between experiments and taken from the in situ CPC measurements for every experiment.

Dust sample	Median diameter, $\bar{D}$ (µm)	Standard deviation, σ_g	Total particle number, N_L
AD1	0.40±0.05	1.70±0.05	measured with in-situ CPC
SD2	0.35±0.05	1.85±0.05	measured with in-situ CPC
ATD	0.35±0.05	1.65±0.05	measured with in-situ CPC

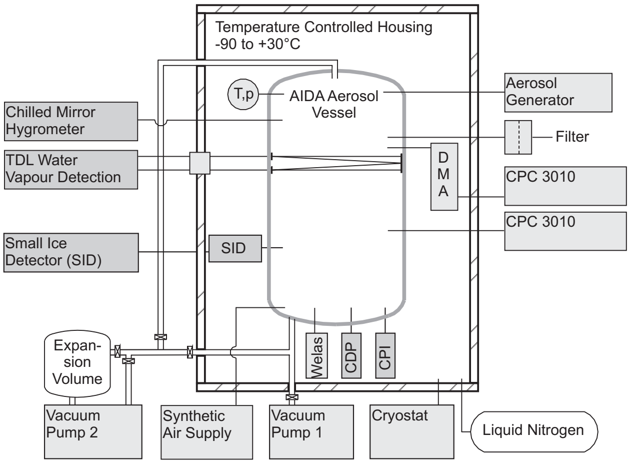

Fig. 1. This shows a schematic of the AIDA facility. The aerosol vessel is cooled inside an insulated cold box by ventilation and liquid nitrogen cooling. A variety of pumps and an expansion volume is used to evacuate the air from the aerosol vessel at different rates, simulating quasi-adiabatic expansion. Dust aerosols are introduced into the chamber using a brush disperser from PALAS and are sampled with a CPC 3010 and the WELAS probe. Total water and water vapour are measured with the chilled mirror and a TDL hygrometer. Cloud particles are sampled with the CPI, the SID, the WELAS and the CDP.

conditions. The AIDA consists of a cylindrical (with rounded ends), 7 m by 4 m, 84 m^3 vessel encased in a large cold box. The vessel itself is connected to a vacuum and air supply system and can be evacuated to a pressure below 0.1 hPa and filled with particle free synthetic air (see Fig. 1). This ensures that background particle concentrations, measured with a condensation particle counter (CPC), are less than 0.1 cm^{-3} (see Möhler et al., 2006).

Experiments are prepared by injecting humid air into the chamber and then slowly cooling throughout the night to the required temperature for the experiment. The reason for the slow cooling of the cold box to the required temperature is that the air can saturate slowly (eventually resulting in frost forming on the interior of the aerosol vessel). The frost coating on the chamber wall results in conditions close to ice saturation at the start of the experiment.

In our experiments dust aerosol samples (AD1, SD2 and ATD) were prepared with a PALAS rotating brush generator in the way described by Möhler et al. (2006, p. 1545) and were introduced into the chamber (see schematic in Fig. 1); a mechanical fan mixed the air at the start of the experiment giving homogeneous conditions within the chamber. Scanning mobility particle sizer (SMPS) measurements conducted separate to this work (Möhler et al., 2006) found the dust particle size distribution (PSD) of the different dust samples to be log-normally distributed in size with fit parameters given in Table 1.

To simulate cloud formation, the chamber volume is expanded using a mixture of Vacuum pump 1, 2 and the expansion volume (see Fig. 1). The time at which the pumps start to expand the volume is set to $t{=}0$ s and typically the experiments last 600 s. Combinations of these pumps to expand the volume are able to yield cooling rates in the chamber (by quasi adiabatic expansion) of up to 4 K min^{-1}. As cooling takes place, conditions of water vapour saturation (liquid or ice) are reached and a cloud is formed on the aerosol particles within the chamber.

The interior wall of the AIDA is ice coated and the temperature of the wall stays relatively constant, while during the experiment the gas is generally colder than the wall. This results in a flux of water vapour from the interior wall of the AIDA to the gas, which is not large, but important enough to significantly alter the relative humidity with respect to liquid water (RH) in the chamber during the expansion.

The aerosol, liquid and ice PSD – 0.5 µm$<D_p<$50 µm – are sampled using the white-light aerosol spectrometer (WELAS) optical particle counter (OPC) from PALAS, which is situated at the bottom of the AIDA vessel (see Fig. 1); total number concentration of particles (0.01 µm$<D_p<$3 µm) is measured with a modified CPC 3010, able to sample at reduced pressures (see Fig. 1).

For a small subset of these experiments we were able to use the small ice detector (SID) probe (Hirst et al., 2001) for sampling the size and concentration of the cloud and for determining cloud phase (liquid or ice). The SID was placed at the side of the AIDA (see Fig. 1). The basis for the discrimination of phase is the assumption that liquid particles are spherical and ice particles are non-spherical. The probe normally uses six detectors arranged azimuthally at a forward scattering angle of 30°, with a seventh detector mounted directly in front of the laser. However, for the AIDA configuration it was decided that one of the azimuthal detectors performed better than the standard design so the probe was configured to use five azimuthal detectors for sizing and shaping and the remaining sixth azimuthal detector for triggering. When a particle passes through the system, the response of scattered light falling on the detectors is recorded. Spherical particles result in light falling relatively uniformly on all five azimuthal signal detectors, while aspherical particles record a non-uniform signal on the detectors. This is quantified by using the asphericity factor, A_f, for each particle measured. The discrimination between liquid and ice particles is fairly clear as two regimes can be seen, liquid having small A_f and ice having large A_f. The A_f is calculated by:

$$A_f = \kappa \frac{\sqrt{\sum_{i=1}^{5}(\langle E\rangle - E_i)^2}}{\langle E\rangle} \tag{1}$$

where κ=22.361, E_i are the detector values and $\langle E\rangle$ is the mean of all detector values. For more information see Sect. 4 of Field et al. (2006) and also Hirst et al. (2001).

A cloud particle imager (CPI) was available for all of the measurements within this paper. The CPI images particles ($10<D_p<2300\,\mu$m) by use of a 20 ns pulsed 100 W laser diode. Images from a charge-coupled device (CCD) camera are recorded with a frame-rate of 40 Hz (see Lawson et al., 2001). The time series of images were used to calculate particle concentrations and the PSD using the calibration method described in Connolly et al. (2007) to correct the raw data. This calibration corrects over sizing and under sampling of the particles relative to their true size by using scalar diffraction theory. Connolly et al. show that using these corrections gives good agreement for the cloud PSD when compared with other cloud spectrometers.

The CPI was placed at the bottom of the AIDA vessel (see Fig. 1) and the airflow through the CPI tube was $\approx$5 ms^{-1}. Asphericity is also the criteria by which CPI images are used to discriminate between liquid or ice. Particles from the CPI that have size greater than 40 µm and a roundness, A_r (see Eq. 2), less than 0.75 and a maximum deviation from the mean radius of 0.1 times the mean radius are classified as ice crystals.

$$A_r = \frac{4 \times \text{Area}}{\pi \times d^2} \tag{2}$$

here, d and Area are the maximum length and the projected area of the particle, respectively.

The chamber also has instrumentation to measure water vapour – a tunable diode laser (TDL) system. The TDL measurement is scaled to the water vapour concentration inferred from the frost point measured by a chilled mirror hygrometer in the absence of cloud. The partial pressure of water vapour is calculated from the frost point using ice saturation vapour pressures by Buck research, which agree within 0.1% of the ice saturation vapour pressure formulation of Murphy and Koop (2005). In some situations it can be seen that there is a systematic error in the values of saturation ratio calculated from the TDL data. These problems are being looked at with on going inter-comparisons between various water vapour probes at the AIDA – they do not affect our conclusions. As mentioned above, we also measured the total water (vapour plus liquid plus ice) using the chilled mirror hygrometer with a heated inlet that evaporated all cloud particles before they entered the sensor. For more information on the instrumental techniques and limitations the reader is referred to Möhler et al. (2006, 2004).

3 Methods of data analysis

3.1 Basic assumptions and definitions

This paper considers the behaviour of the three dust samples in the freezing mode at warmer temperatures than former experiments that investigated the deposition mode of ice nucleation of the same dust samples (Möhler et al., 2006). In contrast to the deposition mode nucleation the freezing mode nucleation is mainly driven by the temperature of the water drops, with no explicit dependence on the water vapour supersaturation.

Our main assumption is that ice nucleation occurs at the interface between a dust particle and the liquid drop it is immersed in. The dust particles are assumed to have a characteristic number density of sites on their surface at which ice germs form at definite temperatures. Our assumption is slightly different to that of Marcolli et al. (2007), who attempted to define a range of nucleation rates for different areas on individual IN using the classical spherical cap model. The main difference being that, in this model, ice crystal formation occurs instantaneously at a defined temperature.

This assumption follows the concept of the singular hypothesis for heterogeneous ice nucleation as described in Sect. 1. The number of these sites per surface area of the dust that are active at temperature T is referred to as the ice-active surface site density (IASSD), and given the symbol $n_s(T)$.

We also define the IASSD that become active as the temperature is lowered by dT and give it the symbol $k(T)$. Note that n_s and k are related by:

$$n_s(T_{\text{min}}) = -\int_0^{T_{\text{min}}} k(T)dT \tag{3}$$

where T_{min} is the minimum temperature reached during the experiment and $k(T)$ is inferred from the experimental data – see Sect. 3.2; $n_s(T_{\text{min}})$ is the IASSD between 0°C and T_{min}. Note also that $k(T)=\frac{dn_s(T)}{dT}$ and is analogous to a time-independent concentration function or "nucleus content" defined by Vali (1971), but in our case has units of germs m^{-2} °C^{-1}.

Now provided the singular hypothesis holds, the rate of change of ice concentration with respect to temperature can be written as:

$$\frac{dN_{i,j}}{dT} = N_{d,j} A_j k(T) \tag{4}$$

where $N_{d,j}$ is the drop number concentration of mass category j (unfrozen), A_j is the surface area of the aerosol in this drop mass category, $N_{i,j}$ is the ice number concentration of drops in category j and $k(T)$ is the IASSD (per unit area of the dust) per temperature interval, which is a function of temperature, T. Note also that the liquid and ice mass grids are assumed to be the same.

Another assumption in this paper is that for a particular dust sample $n_s(T_{\min})$ – the IASSD that form between $T=0$ and $T=T_{\min}$ – is constant for all sizes of the dust sample. Using the same n_s value for all sizes of dust particles may not strictly be valid due to a size dependent mineralogical composition or surface structure. However, for this paper it was deemed acceptable to assume a constant n_s for all sizes to avoid insurmountable complications.

3.2 Using the ice-active surface site density to compute the ice particle concentration in a cloud

We will now consider an experiment (Fig. 2) that starts at temperature T_{init} at sub water saturated conditions (region i, Fig. 2) in which the air is expanded until the point of liquid drop formation on the dust particles at which point the temperature is T_1 and the time is t_1. The air continues to cool by expansion and liquid remains in the cloud (region ii) until time t_2 at temperature T_2 – also referred to as $T_{\min}$. At this time, all of the liquid drops evaporate or freeze and the RH drops below 1.0 (region iii). This is depicted by the schematics in Fig. 2a and b. Note, $T_{\min}$ is not necessarily the minimum temperature of the experiment, but it is the minimum temperature where drops are still present, not having frozen or evaporated.

In order to calculate the time dependent ice particle concentration in this experiment we need to consider two scenarios. (1) is that the IN become active freezing nuclei (i.e. the IASSD is greater than 0) at a time before t_1; (2) is that the IN become active freezing nuclei at t_1<time<t_2. These two scenarios are depicted in Fig. 2c and e with the corresponding ice particle number concentrations in Fig. 2d and f. We will refer back to this "experiment" throughout this section.

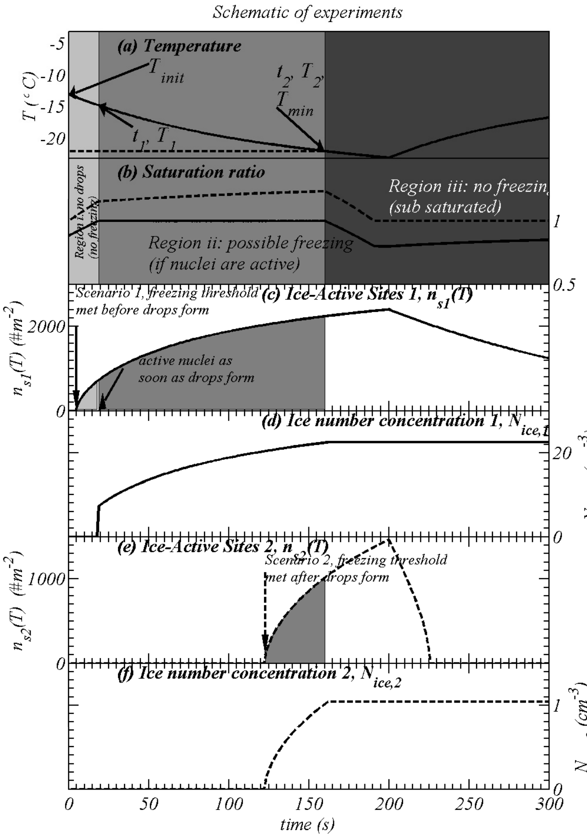

Fig. 2. A schematic of the freezing experiments to illustrate how the ice concentration is calculated. **(a)** shows a temperature time series starting at $t=0$, with decreasing temperature until time t_1 is reached at temperature T_1, where the saturation ratio, $s_w=1.0$ – see **(b)**. The cooling continues, with ice forming until s_w goes below 1.0 and all drops evaporate at time t_2, temperature, T_1, or $T_{\min}$. After this point, no more ice can form from the freezing of drops. **(c)** shows a hypothetical value for IASSD, in this scenario the value is above zero before drops form (in region i) and consequently as soon as the drops form they start to freeze instantly and then continuously as the temperature is decreased further (region ii). **(d)** shows the corresponding ice particle number concentration for Scenario 1. **(e)** shows the same but for a scenario where the value is zero until some time after drops form; in this case the ice crystals start to form continuously, part way through region iii, when the temperature threshold for nucleation is met. **(f)** shows the corresponding ice particle number concentration for Scenario 2.

In order to calculate the time dependent formation rate of ice crystals we can multiply Eq. (4) by the cooling rate to obtain time derivatives (instead of wrt. temperature):

$$\frac{dN_{i,j}}{dt} = N_{d,j} A_j k(T) \frac{dT}{dt} \tag{5}$$

substituting $k(T)=-\frac{dn_s(T)}{dT}$ into Eq. (5) and integrating yields:

$$N_{i,j}(t_1 \to t_2) = \Delta N(T_1) + \int_{t=t_1}^{t=t_2} N_{d,j} A_j \frac{dn_s(T)}{dT} \frac{dT}{dt} dt \tag{6}$$

here, $\Delta N(T_1)$ is the number of ice crystals formed by active IN between 0°C and T_1, where T_1 is the temperature when the drops first formed. This is the case for scenario 1 described above where IN are potentially active at times $<t_1$. In scenario 1, even though the IN are potentially active for times $<t_1$, no ice particles can form because there are no liquid drops present; however, when liquid drops form at time $=t_1$, this built-up reservoir of potential IN becomes active instantly (the reservoir is shown by the light-grey shading in Fig. 2c).

In order to compute this ΔN term we note that initially the only important transformation process affecting number concentrations of aerosol and ice crystals is the formation of ice particles; aggregation, coalescence and washout are negligible. Therefore we can substitute $N_d{=}N_s{-}N_i$ – here, N_d and N_i are the drop and ice particle number concentrations, respectively; N_s is the starting number of drops (constant with time) – in Eq. (4) and integrate wrt. T.

$$\frac{dN_i}{dT} = (N_s - N_i)Ak(T) \tag{7}$$

integrating Eq. (7) yields an equation for the number of ice crystals at time $=t_1$:

$$\int_0^{N_i} \frac{1}{N_s - N_i} dN_i = A \int_0^{T_1} k(T)dT \tag{8}$$

or

$$N_i(0 \rightarrow t_1) = \Delta N = N_s(1 - \exp[-An_s(T_1)]) \tag{9}$$

where

$$n_s(T_1) = -\int_{T=0}^{T=T_1} k(T)dT \tag{10}$$

For times $>t_1$, the increase in ice particle number concentration can be computed from the second term on the rhs of Eq. (6). This results in the IASSD increasing wrt. time (denoted by the darker shading in Fig. 2c).

For scenario 2, where IN become active after t_1, the ice particle number concentration is also computed from the second term on the rhs of Eq. (6) but there is no need to calculate the ΔN term.

3.3 Deriving the dependence of the ice-active germ density on temperature

3.3.1 Heterogeneous freezing

The main tool used in this analysis is the aerosol-cloud-precipitation interaction model (ACPIM), which has been developed at the University of Manchester (UoM) in collaboration with the Forschungszentrum Karlsruhe; it is described in the Appendix.

In order to derive the value of n_s we adopted the following method – note the actual AIDA experiments in general followed the same life cycle to the schematic experiment described in Fig. 2. For every experiment in Tables 2, 3 and 4 (see Sect. 4) we initialised ACPIM with the aerosol PSD parameters in Table 1 with the total aerosol number from the in situ CPC measurements. We then constrained the ACPIM to the measured time-series of T, P and total water mass content as described in the Appendix. The drop number concentration was predicted by the ACPIM model and we calculated the surface area of dust in contact with the liquid drops in the model. The ice formation rate in the ACPIM was constrained to the measured ice formation rate with the CPI (see Sect. 2.1). This enabled us to calculate the time series of the product of the IASSD per temperature interval, $k(T)$, and the cooling rate, $\frac{dT}{dt}$. The product $k(T)\frac{dT}{dt}$ can be calculated by rearranging Eq. (5):

$$k(t)\frac{dT}{dt} = \sum_j^M \frac{dN_{i,j}}{dt} \Big/ \sum_j^M (N_{d,j} \times A_j) \tag{11}$$

Equation (11) was then integrated between times t_1 and t_2 (which is equivalent to the integral in Eq. 3) to yield the IASSD, $n_s(T_{\text{min}})$. This method was repeated for all the experiments providing enough points to fit a polynomial to n_s vs. T_{min}. Admittedly other functional forms could also be used with this method, but we decided on a polynomial as it fitted the data well enough.

There are other ways that could have been used to estimate n_s, for instance, one could estimate the surface area of dust in contact with the drops by finding the average surface area of the dust distribution via Table 1 (i.e. the second moment of the dust distribution) and inverting Eq. (9), therefore not requiring a model. However, we feel our method is the best for this application.

An advantage of our method is that we are able to take into account the modelled surface area of dust in contact with individual drops. For instance the larger dust particles freeze the drops first as they contain larger surface area – and thus a larger IASSD (meaning that the average surface area in the drops decreases with time); also, the larger dust particles activate as cloud condensation nuclei (CCN) before the smaller particles so adding flaws to the assumption that the surface area of the dust in contact with the drops is just the average surface area of the distribution in Table 1.

3.3.2 Heterogeneous deposition

In some experiments, where RH<1.0, on ATD we noted significant nucleation due to heterogeneous deposition and in this case we inferred the IASSD n_s as a function of supersaturation with respect to ice, s_i. The theory used is analogous to that described in Sect. 3, except that all occurences of temperature, T, are substituted for ice supersaturation, s_i. Also instead of the minimum temperature reached determining the IASSD it is the maximum ice supersaturation reached $s_{i,\text{max}}$ during the experiment – i.e. $n_s(s_{i,\text{max}})$. Since heterogeneous deposition does not require the presence of water drops the ΔN in the analogous Eq. (6) is set to zero for the case of heterogeneous deposition.

3.4 Quality control

This last step was performed to quality control the derived parameterisations of n_s. We therefore ran the ACPIM in a purely predictive mode, initialised with the dust PSD – see Table 1 – and still constrained to the timeseries of T, P and total water mass content. The model was used to predict the

Table 2. Experiments for AD1 dust. Dual refers to the fact that deposition was observed before the formation of liquid.

Date	Experiment	T_{min}	Liquid Observed	Comments
24 September 2003 10:30:00	IN04_18	−30.0°C	Yes	Freezing
24 September 2003 12:15:02	IN04_19	−32.0°C	Yes	Freezing
24 September 2003 14:00:01	IN04_20	−32.0°C	Yes	Freezing
24 September 2003 15:45:00	IN04_21	−33.5°C	Yes	Freezing
16 November 2004 10:30:00	IN05_51	−27.0°C	Yes	Freezing
16 November 2004 12:45:00	IN05_52	−21.8°C	Yes	Dual
17 November 2004 10:30:00	IN05_55	−27.5°C	Yes	Freezing
17 November 2004 12:50:00	IN05_56	−18.5°C	Yes	Dual – very low
23 September 2003 10:31:40	IN04_15	−5.5°C	Yes	No Ice
23 September 2003 12:16:40	IN04_16	−6.5°C	Yes	No Ice
12 November 2004 11:10:00	IN05_45	−12.5°C	Yes	No Ice
12 November 2004 15:05:00	IN05_46	−12.5°C	Yes	No Ice
12 November 2004 16:30:00	IN05_47	−12.4°C	Yes	No Ice
15 November 2004 10:45:00	IN05_48	−18.5°C	Yes	Some ice by dep.
15 November 2004 12:40:00	IN05_49	−18.1°C	Yes	No Ice

Table 3. Experiments for SD2 dust. Low aerosol refers to a case where ice was observed, but the statistics were poor due to low aerosol concentrations. This experiment was not used in the analysis.

Date	Experiment	T_{min}	Liquid Observed	Comments
17 September 2003 10:50:00	IN04_06	−27.5°C	Yes	Freezing
17 September 2003 12:16:00	IN04_07	−25.5°C	Yes	Freezing
29 September 2003 10:31:00	IN04_30	−26.3°C	Yes	Freezing
29 September 2003 12:15:00	IN04_31	−26.0°C	Yes	Freezing
–	IN04_32	–	Yes	Low aerosol
18 November 2004 10:35:00	IN05_58	−26.7°C	Yes	Freezing
18 November 2004 12:45:00	IN05_59	−25.5°C	Yes	Freezing
15 September 2003 11:50:00	IN04_01	−1.5°C	Yes	No Ice
15 September 2003 17:05:00	IN04_02	−2.9°C	Yes	No Ice
16 September 2003 14:01:00	IN04_03	−4.7°C	Yes	No Ice
16 September 2003 15:45:00	IN04_04	−7.8°C	Yes	No Ice
17 September 2003 10:50:00	IN04_05	−8.3°C	Yes	No Ice
10 November 2004 12:45:00	IN05_40	−5.0°C	Yes	No Ice
10 November 2004 14:15:00	IN05_41	−6.9°C	Yes	No Ice

drop and ice particle concentration and the RH. The ice particle concentration was predicted with Eq. (6) and the derived n_s polynomials. These were compared visually with the measurements in order to assess the validity of smoothing of data with a polynomial function.

4 Results

The results are from three separate sets of experimental campaigns lasting approximately 2 weeks each: IN02 in 2002, IN04 in 2003 and IN05 in 2004. Summaries of the experiments used in the analysis are shown in Tables 2, 3 and 4.

4.1 Intercomparison of SID and CPI derived ice-active germ densities

For small crystals the SID is better than the CPI for phase discrimination; however, in experiments where the ice crystals grow rapidly outside of the range observable by the SID the CPI is the better of the two instruments for determining ice number concentrations providing the correction algorithms of Connolly et al. (2007) are used.

The SID measurements were only available for a limited number of experiments during IN04 and it is desirable to use the larger, more complete dataset of the CPI, collected for our experiments, for determining ice concentrations. However,

Table 4. Experiments for ATD dust. Low aerosol refers to a case where ice was observed, but the statistics were poor due to low aerosol concentrations. This experiment was not used in the analysis. Homogeneous freezing refers to an experiment where the supercooling was below that required for homogeneous freezing to take place.

Date	Experiment	$T_{\min}$	Liquid Observed	Comments
17 September 2003 16:30:00	IN04_09	−27.9°C	Yes	Freezing
17 September 2003 17:30:00	IN04_10	−26.2°C	Yes	Freezing
04 July 2002 15:04:00	IN02_74	–	No	Homogeneous freezing
05 July 2002 13:38:00	IN02_79	−27.0°C	Yes	Freezing
08 July 2002 11:45:00	IN02_83	−19.3°C	Yes	Freezing
08 July 2002 13:30:00	IN02_84	−18.1°C	Yes	Freezing
08 July 2002 14:42:00	IN02_85	−18.0°C	Yes	Freezing
08 July 2002 16:00:00	IN02_86	−17.9°C	Yes	Freezing
08 July 2002 16:57:00	IN02_87	−17.9°C	Yes	Freezing
11 July 2002 15:10:00	IN02_103	−12.4°C	Yes	No Ice
11 July 2002 16:30:00	IN02_104	−12.0°C	Yes	No Ice
04 July 2002 11:46:00	IN02_72	−34.5°C	No	Deposition
04 July 2002 13:18:00	IN02_73	−33.7°C	No	Low aerosol
04 July 2002 17:51:00	IN02_75	−34.9°C	No	Deposition
05 July 2002 10:35:00	IN02_77	−27.9°C	No	Deposition
05 July 2002 11:34:00	IN02_78	−26.5°C	No	Deposition
05 July 2002 14:48:00	IN02_80	−26.0°C	No	Deposition
05 July 2002 16:11:00	IN02_81	−25.0°C	No	Deposition

since the CPI cannot observe the smallest ice crystals nucleated at the start of the experiment we need to validate the CPI against the SID.

Figure 3 shows a comparison of the IASSD calculated with both probes with error bars[1]. The comparison shows good linear agreement between the two methods with the CPI tending to under predict the IASSD when compared to the SID probe. It is not clear whether this is due to problems with SID, CPI or both and so the offset should be kept in mind.

The Poisson uncertainty associated with the CPI data are larger than the SID errors and are partly because the airflow velocity was lower though the CPI ($5\,\mathrm{m\,s^{-1}}$) than it was through the SID ($10\,\mathrm{m\,s^{-1}}$) and also because the sample volume of the CPI is smaller than SID due to probe dead-time.

4.2 Determination of ice-active germ density vs. T

The CPI data was used to infer the IASSD, $n_s(T)$, as a function of temperature in the manner described in Sect. 3.3. Figure 4 shows the results of this analysis for these experiments. For freezing on AD1 (Fig. 4a) we can see that the IASSD is negligible for temperatures warmer than −18°C and increases only gradually to temperatures of −27°C. Note that experiments IN05_45, 46, 47, 48 and 49 were performed for temperatures warmer than this (−12.5°C) and yielded no ice crystals (see Table 2). The IASSD increases markedly at temperatures less than −30°C.

A polynomial fit to the data for AD1 is shown by the grey dashed line and yields the following curves for $T>-33$°C:

$$n_s(T)=\begin{cases} a_1(T+a_2)^2, & T<-a_2 \\ 0, & T\geq -a_2 \end{cases} \tag{12a}$$

$$\frac{dn_s(T)}{dT}=\begin{cases} -k(T)=2\times a_1(T+a_2), & T<-a_2 \\ -k(T)=0, & T\geq -a_2 \end{cases} \tag{12b}$$

Here, a_1=6.723780×10^9, a_2=2.078×10^1 C.

For freezing on SD2 (Fig. 4b) the range in temperature for the data was unfortunately not as large as for the AD1 sample. If we look at the enlarged plot (Fig. 4b(ii)), we can see that the trend is for increasing IASSD with decreasing temperature.

It should be noted that experiments were performed at warmer temperatures ($-1.5<T\leq 8.5$°C) than this (experiments IN04_01, 02, 03, 04 and 05) and non of them yielded any ice to within the detection limits of the experiment (see Table 3). A polynomial fit to the data for SD2 is shown by the grey dashed line and when fitted to Eq. (12) for $T>-26.8$°C yields a_1=4.315221×10^{10}, a_2=2.503×10^1 C. Note that the fitted curve is zero for $T>-25.03$°C unlike the data, which shows small, but finite values for n_s warmer than −25°C.

For freezing on ATD (Fig. 4c) we noted that there was no freezing at temperatures warmer than −18°C to within detection limits (this was also confirmed by experiments

---

[1] The error bars assume Poisson counting errors at 5 and 95% confidence.

IN04_103 and IN02_104 at temperatures of −12°C). At temperatures colder than this there was a gradual increase in the IASSD. For the same temperatures, the freezing mode on ATD showed the highest IASSD compared to the other two desert dusts. A polynomial fit to the data for ATD is shown by the grey dashed line and when fitted to Eq. (12) for $T > -27°\mathrm{C}$ yields $a_1 = 2.019153 \times 10^9$, $a_2 = 1.515 \times 10^1$ C.

No heterogeneous freezing was observed on ATD for experiments that started at temperatures colder than −24°C and this was probably due to the fact that heterogeneous deposition became very efficient at temperatures colder than −25°C, as evident in experiments IN02_72, 73, 75, 77, 78, 80 and 81 (see Table 4). This creates a large vapour sink to the particles and impedes liquid drop formation.

Figure 4d shows results at two different temperatures for deposition nucleation on ATD – see Sect. 3.3.2. The lines with triangles show experiments at −33°C and lines with pluses show experiments at −25°C. Experiment 81 reached a lower supersaturation (s_i=0.16) with respect to ice than experiment 80 (s_i=0.21) and yet shows a higher IASSD ($0.5 \times 10^{11}\,\mathrm{m}^{-2}$ against $0.37 \times 10^{11}\,\mathrm{m}^{-2}$). Both values are within the Poisson uncertainty at the 90% level and we cannot say if there are pre-nucleation effects occurring between IN02_80 and IN02_81.

For the heterogeneous deposition experiments in Fig. 4d the dependence of IASSD on ice supersaturation is consistent with the analysis at Ci temperatures by Möhler et al. (2006).

4.3 Testing the parameterization

The IASSD determined in the previous section (see Fig. 4a–c) were quality controlled using the ACPIM model in a predictive mode as described in Sect. 3.4.

Our aim was to test the parameterizations for experiments observed at both extremes of the curves for n_s in Fig. 4 – i.e. experiments near the onset of ice formation and examples at the low temperature end of the parameterization. We have done this by visually comparing the concentration timeseries from the model and data. Note that toward the end of all experiments the measured ice concentration decreases whereas the modelled value stays constant. The reasons for this are (1) fall out of the largest crystals to the chamber floor as they grow to large sizes; and at the very end (2) sublimation of some ice crystals to sizes not observable by the instruments.

4.3.1 ATD

Firstly we shall evaluate the ATD n_s against T curve (Fig. 4c) by looking at experiments IN02_86 and IN04_10. IN02_86 started at −10.8°C and during the experiment the temperature was reduced to −17.9°C (see Fig. 5a). Liquid drops formed at about t=140 s following which some of them froze. The ice crystal habits observed with the CPI in this experiment were similar to the overlapping parallel plates observed by Bailey and Hallett (2004) in experiments at −20°C (see Fig. 5, right panel).

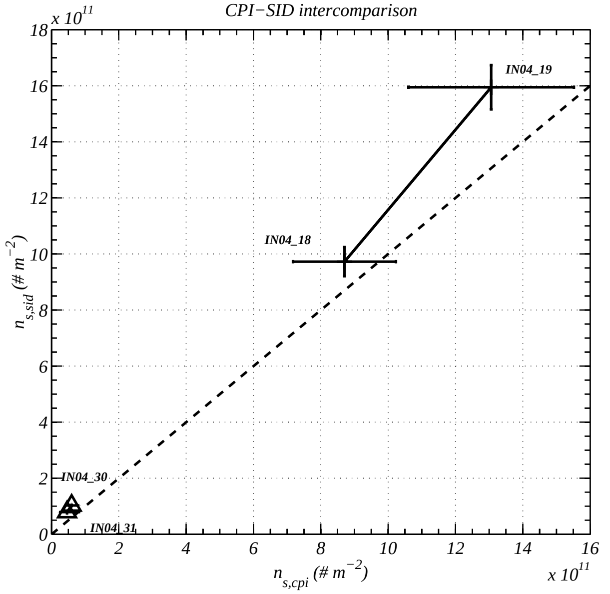

Fig. 3. This shows an inter-comparison of calculated IASSD between CPI and SID for the available experiments. Error bars are 5 and 95 confidence limits for a Poisson distribution. It can be seen that the errors associated with the CPI data are higher than the SID. This is mainly because a lower air velocity was used to calculate the errors in counting with the CPI. Also, there is in general a tendency for the CPI to undercount ice crystals relative to the SID probe. It is not clear whether this is a problem with SID or the CPI but it should be kept in mind when considering the results.

It can be seen that there is reasonable agreement between the modelled ice concentration and that observed with the CPI ($0.1\,\mathrm{cm}^{-3}$ and $0.25\,\mathrm{cm}^{-3}$, respectively). The starting total water concentration has to be increased[2] in this simulation relative to that measured so that the simulated appearance of drops was in accord with the observations from the CPI.

The IN04_10 experiment started at −19°C and during the experiment the temperature was reduced to −26°C (see Fig. 6a, left panel). Liquid drops formed at about t=80 s (see the WELAS plot – Fig. 6f) and no significant freezing was observed with either the CPI (Fig. 6b) or SID (Fig. 6c) until about t=130 s. The ice crystal habits observed in this experiment were similar to side planes, overlapping parallel plates and possibly bare spearheads observed by Bailey and Hallett (2004) at −20 and −30°C.

It appears that in Fig. 6b and c the model over-predicts the concentration of ice crystals initially, but the concentrations agree at the end of the IN04_10 experiment. Also evident in

---

[2] The cause of this is a systematic error (i.e. offset) in the instrument that measures total water. The implications for the quality of the simulation are insignificant.

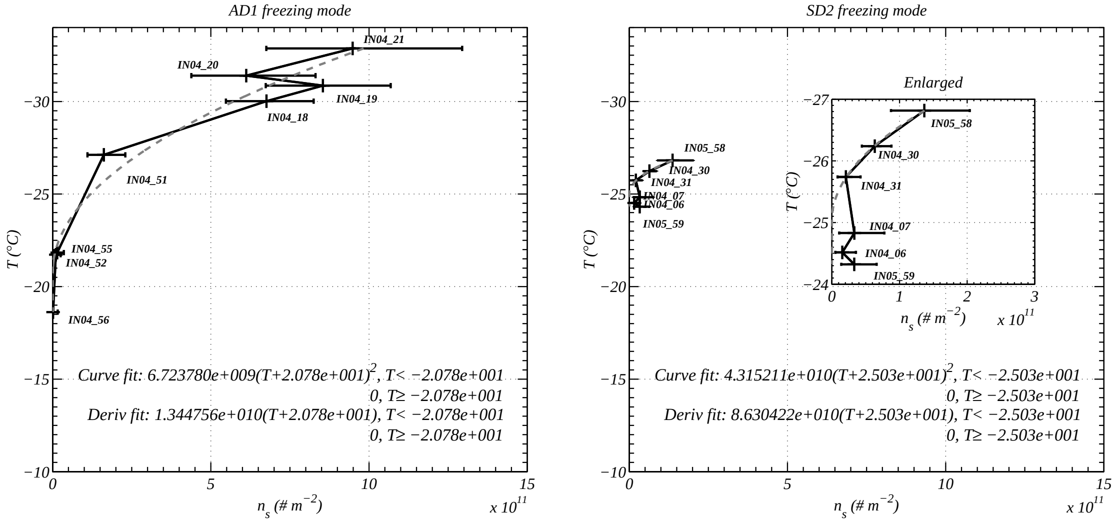

(a) Freezing on AD1 (b) Freezing on SD2

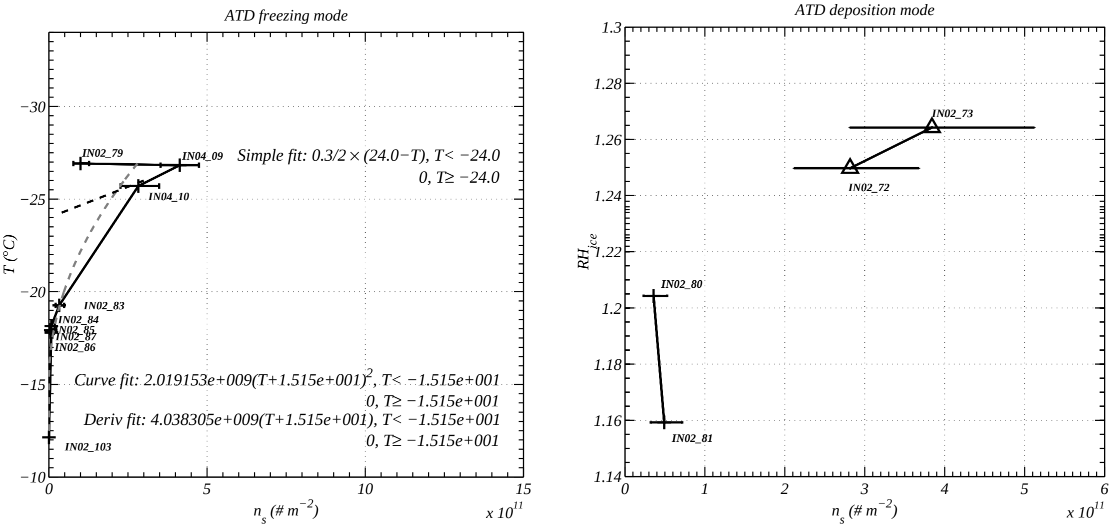

(c) Freezing on ATD (d) Deposition on ATD

Fig. 4. This shows results from the ice nucleation experiments in the AIDA. **(a)** shows the curve of IASSD between 0°C and the temperature on the y-axis for AD1; in all graphs, error bars assume 5 and 95 confidence intervals of the Poisson distribution based on the ice concentration from the CPI. The gray dashed line shows a robust fit to the data and equations for the curves and their derivatives wrt. T are shown for the freezing experiments. **(b)** (i) shows the same for IASSD between 0°C and the temperature on the y-axis for SD2, while **(b)** (ii) is an enlargement of this. **(c)** shows the same for IASSD between 0°C and the temperature on the y-axis for ATD. For this experiment the fit did not yield good agreement with the data since there was a large gap in measurements between −18 and −25°C. A simple visual fit (shown by the black dashed line) yielded a good comparison with the experiments. **(d)** shows the IASSD between 0 and $\mathrm{RH}_{\mathrm{ice}}$ on the y-axis for ATD in experiments below water saturated conditions (i.e. nucleation due to heterogeneous deposition).

Fig. 6e is the fact that the modelled supersaturation with respect to ice is too low when compared to the water vapour TDL measurement after t=150 s, which also suggests problems with the prediction of the ice crystal concentration. This has the effect of evaporating the liquid drops in the model too quickly: there are no drops after t=130 s in the model, but in the observations they last until t=220 s.

The reason for this poor agreement seems to be due to the fact that there is missing data in the freezing curve parameterisation in the temperature regime −20 to −25°C (see

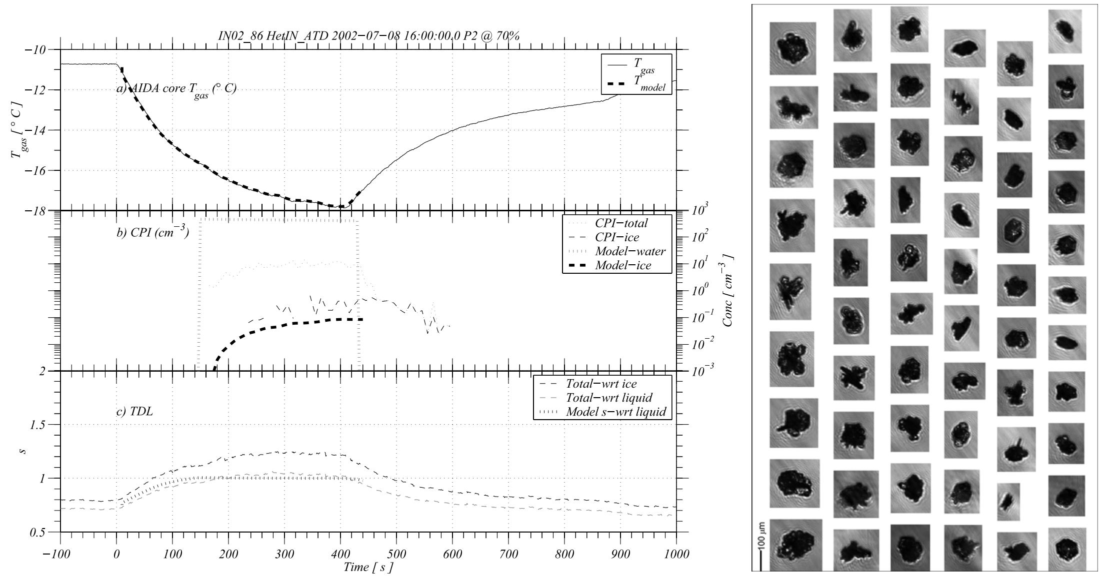

Fig. 5. Experiment IN02_86 showing freezing on ATD at −16°C. **(a)** shows the measured (black line) and modelled air temperature (thick black dashed line); **(b)** shows the CPI measured total concentration (grey dotted line) and ice (black solid line), the modelled liquid and ice concentrations are shown by the thicker dotted grey and dashed black lines, respectively; **(c)** shows the measured total water content converted to an equivalent saturation ratio wrt. ice (black dashed line) and saturation wrt. liquid (grey dashed line), the thicker dotted line is the modelled RH (no TDL measurements were available for this experiment). Ice crystal images observed are shown on the right.

Fig. 4c). If we use a different freezing curve that also fits the data well, but has a lower IASSD at −24°C, we are able to get better agreement. This curve is shown by the black dashed line in Fig. 4c and is given by Eq. (13)

$$n_{s,\mathrm{ATD}}(T) = \begin{cases} \frac{0.3\times 10^{12}}{2} \times (2.4\times 10^{1} - T), & T < -2.4\times 10^{1}\,^{\circ}\mathrm{C} \\ 0, & T \geq -2.4\times 10^{1}\,^{\circ}\mathrm{C} \end{cases} \quad (13)$$

Figure 7 shows the result of using the above equation instead of the fitted polynomial in Sect. 4. We see that there is much better agreement with the ice concentration, drop concentration and RH.

4.3.2 AD1

We shall now evaluate the AD1 curve by looking at experiments IN05_51 and IN04_18, since these experiments were performed at 2 quite different temperatures (see Fig. 4a). IN05_51 started at −17.5°C and during the experiment the temperature was reduced to −27.5°C (see Fig. 8a). Liquid drops formed at about t=40 s following which there was a small amount of freezing. The ice crystal habits observed in this experiment were quite similar to those observed on ATD during experiment IN04_10; that is similar to the side planes, overlapping parallel plates and possible bare spear heads observed by Bailey and Hallett (2004) at −20°C and −30°C (see Fig. 8, right panel).

There is very good agreement between the modelled ice concentration and the observed CPI concentration with both showing around 2 cm^{-3} of ice crystals near the end of the experiment (t=300 s). For this simulation, the total water content had to be slightly adjusted in the model from that measured so that liquid water appeared at the correct time. This can be seen by the offset between the modelled RH and the measured RH at t=40 s (see Fig. 8c). The total concentration measured from the WELAS OPC agrees reasonably well with the concentration of drops at the start of liquid drop formation (see Fig. 8d).

Experiment IN04_18 started at −20°C and during the experiment the temperature was reduced to −30°C (see Fig. 9a, left panel). Liquid drops formed at about t=140 s (see the WELAS plot – Fig. 9f) and freezing was observed to commence just after t=150 s as was evident from the CPI and SID time series (Fig. 9b and c). The crystals in this experiment were small and it is almost impossible to tell what they are from the CPI imagery (Fig. 9, right panel); but they are likely to be overlapping parallel plates like observed in IN05_51.

The starting total water content had to be adjusted slightly[3] in the simulations from the observed value in order that liquid water in the model appeared at the same time as that observed with the WELAS probe (see Fig. 9f). However, in

---

[3] The cause of this is a systematic error (i.e. offset) in the instrument that measures total water. The implications for the quality of the simulation are insignificant.

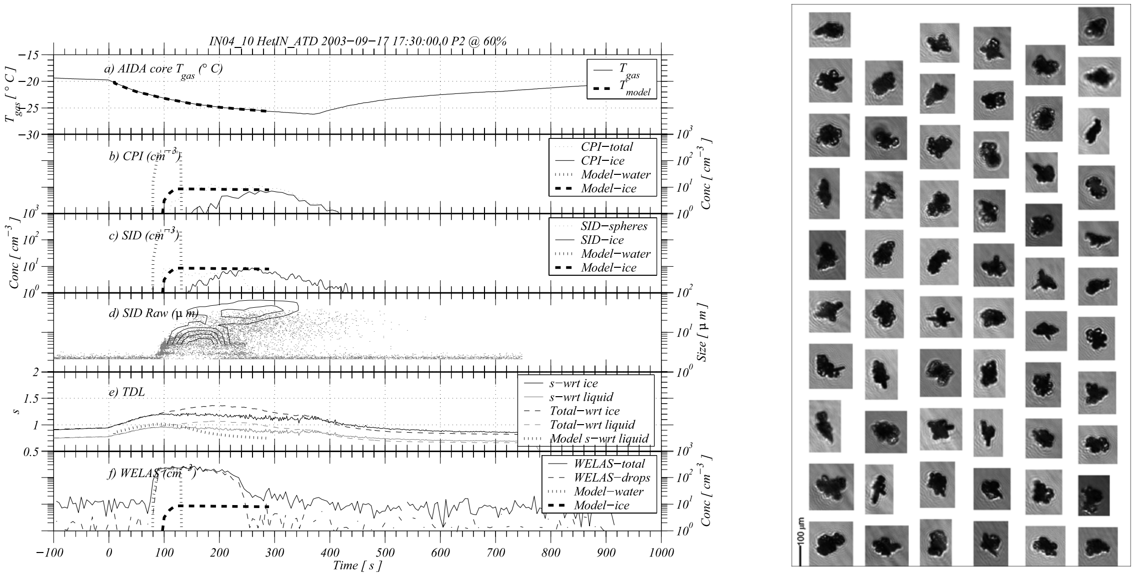

Fig. 6. Experiment IN04_10 showing ice nucleation on ATD at −24°C. **(a)** shows the measured (black line) and modelled air temperature (thick dashed line); **(b)** shows the CPI measured total concentration (grey dotted line) and ice (black solid line), the modelled liquid and ice concentrations are shown by the thicker dotted grey and dashed black lines, respectively; **(c)** shows the SID concentrations: grey dotted line is total liquid, black solid line is ice cloud and the modelled liquid and ice concentrations are shown by the thicker dotted grey and dashed black lines, respectively. **(d)** shows the individual counts of particle size from the SID probe and over laid concentration contours from the CPI. **(e)** shows the measured saturation ratio and total water content converted to an equivalent saturation ratio: solid black line is the saturation ratio wrt. ice, grey solid line wrt. liquid, while the black dashed line is the total water content saturation ratio wrt. ice and the grey dashed line wrt. liquid. The modelled saturation ratio wrt. liquid is shown by the thicker black dotted line. **(f)** shows the WELAS concentration: black solid line is total concentration (aerosol+cloud), and grey dashed line is the cloud concentration. The modelled liquid and ice concentration are shown by the thicker grey dotted and black dashed lines, respectively. Ice crystal images observed are shown on the right.

comparison with other experiments the starting RH was low in this experiment and is the reason why the ice crystals do not grow to be so large. Figure 9d shows individual size inferred from the SID probe with the PSD contours from the CPI overlaid; these too show good agreement. In this experiment we have good agreement for the concentration of ice and the times at which liquid appears and evaporates. This suggests that the parameterized curve that was fitted (Fig. 4a) describes the data quite well.

4.3.3 SD2

We shall now evaluate the SD2 curve by looking at experiments IN05_58 and IN04_31, since these experiments were performed at 2 different temperatures within the range of observations (see Fig. 4b). IN04_31 started at −17°C and during the experiment the temperature was reduced to −26°C (see Fig. 10a). Liquid drops formed at about t=50 s following which there was a very small amount of freezing. The ice crystal habits observed in this experiment were quite similar to those observed on ATD during experiment IN04_10; that is similar to the side planes, overlapping parallel plates and possible bare spear heads observed by Bailey and Hallett (2004) at −20°C and −30°C, but there were only a small amount of crystals in total (see Fig. 10, right panel).

There is very good agreement between the modelled ice concentration and the observed CPI concentration with both showing around 0.1 cm^{-3} of ice crystals near the end of the experiment (t=300 s). However, near the start of the experiment, just after liquid drops form at t=50 s, the SID probe observes low concentrations of small ice crystals. The reason these crystals are not nucleated in the model is because the value of n_s in the polynomial fit is zero in this temperature regime; however, the data does show low values of IASSD of about $0.1\times10^{11}\,\text{m}^{-2}$ (see Fig. 4b). For predictions of ice number concentration in this temperature regime on SD2, a value of n_s=$0.1\times10^{11}\,\text{m}^{-2}$ could be used instead of the curve.

For this simulation, the total water content had to be slightly adjusted in the model from that measured so that liquid water appeared at the correct time. This can be seen by the offset between the modelled RH and the measured RH at t=40 s (see Fig. 10e). The total concentration measured from the WELAS OPC agrees reasonably well with the concentration of drops at the start of liquid drop formation

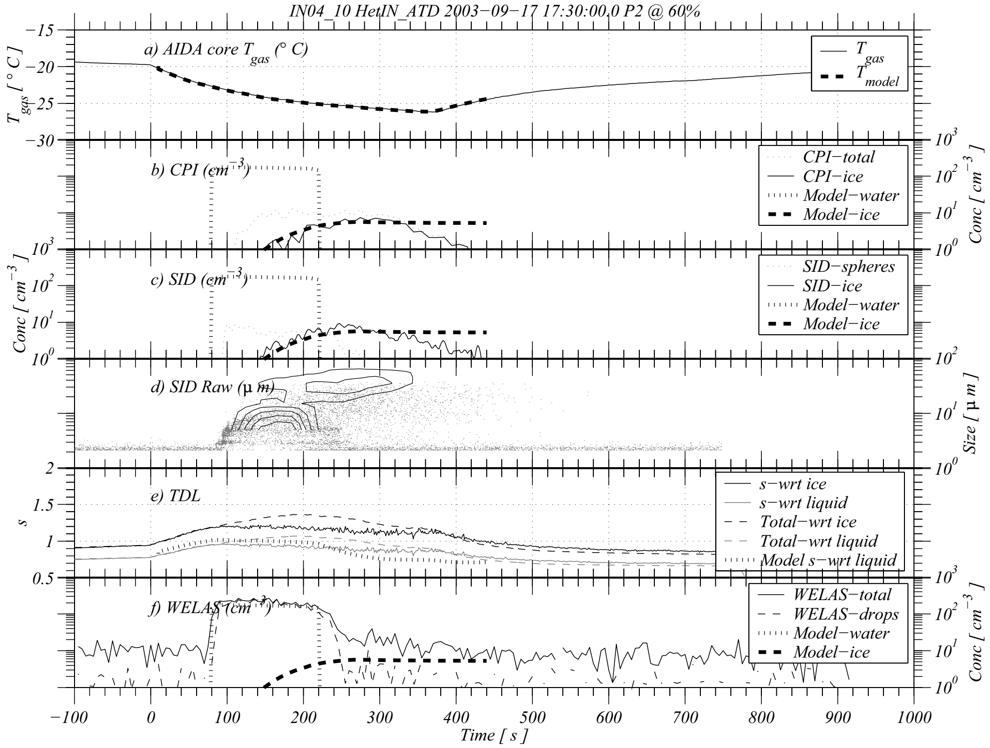

Fig. 7. Experiment IN04_10 showing ice nucleation on ATD using a better fit. Plot captions are as for Fig. 6

(see Fig. 10f) and the sizes of individual particles from the SID probe agree well with the PSD contours from the CPI (Fig. 10d shows these sizes with the contours of the CPI PSD overlaid in black).

Experiment IN05_58 started at −17.5°C and during the experiment the temperature was reduced to −27°C (see Fig. 11a, left panel). Liquid drops formed at about t=40 s (see the WELAS plot – Fig. 11d) and freezing was observed to commence just after t=150 s as was evident from the CPI time series (Fig. 11b). The crystals in this experiment had the appearance of overlapping parallel plates, and bare spear heads, consistent with ice crystal habits observed by Bailey and Hallett (2004) at −20 and −30°C (see Fig. 11, right panel).

The starting total water content had to be adjusted slightly[4] in the simulations from the observed value in order that liquid water in the model appeared at the same time as that observed with the WELAS probe (see Fig. 11c and d). The total cloud concentration measured with the WELAS OPC shows good agreement with the modelled drop concentration also. In this experiment we have good agreement for the concentration of ice and the times at which liquid appears and evaporates. This suggests that the parameterized curve that was fitted (Fig. 4c) describes the data reasonably well; however, in the regime where $-24.4 > T > -25.8$°C, n_s should be set to a constant (0.1×10^{11} m^{-2}).

4.4 Characterization of SD2 and ATD composition

It is clear that the three dusts exhibit different nucleation efficiencies at the 90% certainty level, as noted by the Poisson uncertainties in Fig. 15a–c. The purpose of this analysis was to see if any large differences could be attributed to the elemental composition of the dust samples.

An analysis of the elemental composition of Saharan mineral dusts similar to those used here has been presented previously (Linke et al., 2006). This analysis was provided by X-Ray Fluorescence Analysis (XRF, Bruker AXS, SRS 303AS) for bulk samples preheated to 1000°C and for particle sizes D_p<20 µm. Here we will focus briefly on specific aspects of a further morphological and elemental composition analysis conducted on samples of SD2 and ATD using an environmental scanning electron microscope (ESEM) – Phillips XL30 ESEM-FG – which was used to isolate and image individual dust particles. Target images were then compared with spectra collected using the ESEM associated energy dispersive X-ray (EDX) analysis system. Dust samples were mounted onto a standard aluminium stub following dispersal onto double sided carbon film. Excess dust was blown or vibrated off the film. ESEM images were then taken of an area of the stub where an even and almost complete coverage by dust particles was observed.

---

[4] The cause of this is a systematic error (i.e. offset) in the instrument that measures total water. The implications for the quality of the simulation are insignificant.

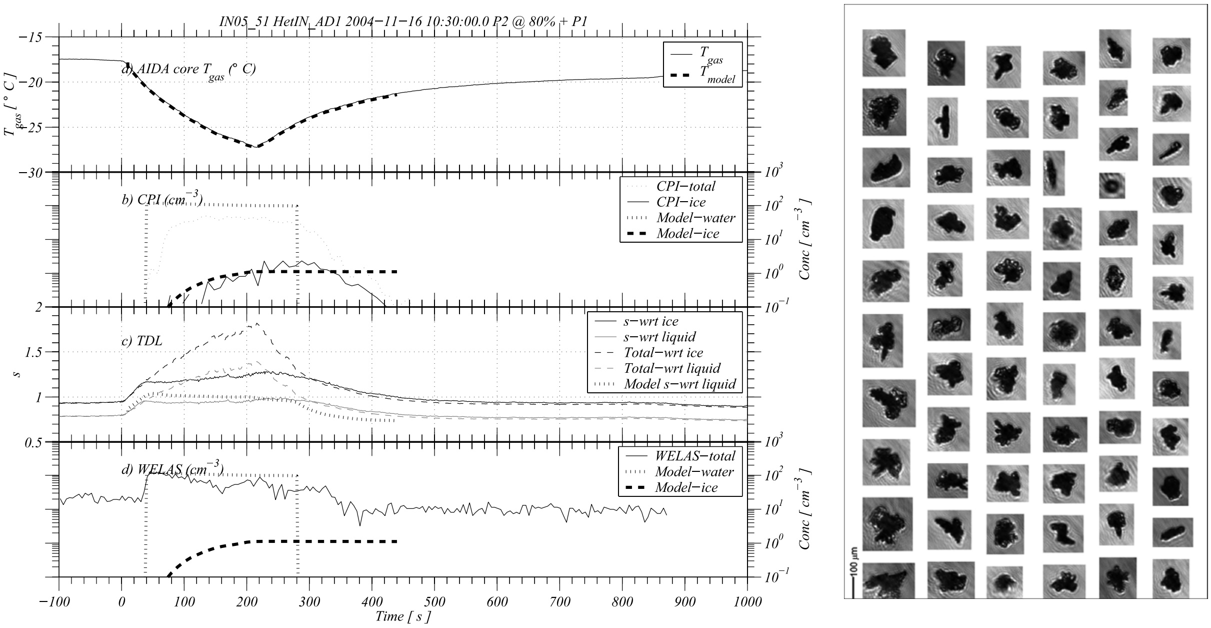

Fig. 8. Experiment IN05_51 showing freezing on AD1 at −22°C. **(a)** shows the measured (black line) and modelled air temperature (thick dashed line); **(b)** shows the CPI measured total concentration (grey dotted line) and ice (black solid line), the modelled liquid and ice concentrations are shown by the thicker dotted grey and dashed black lines, respectively; **(c)** shows the measured saturation ratio and total water content converted to an equivalent saturation ratio: solid black line is the saturation ratio wrt. ice, grey solid line wrt. liquid, while the black dashed line is the total water content saturation ratio wrt. ice and the grey dashed line wrt. liquid. The modelled saturation ratio wrt. liquid is shown by the thicker black dotted line. **(d)** shows the WELAS concentration: black solid line is total concentration (aerosol+cloud). The modelled liquid and ice concentration are shown by the thicker grey dotted and black dashed lines, respectively. Ice crystal images observed are shown on the right.

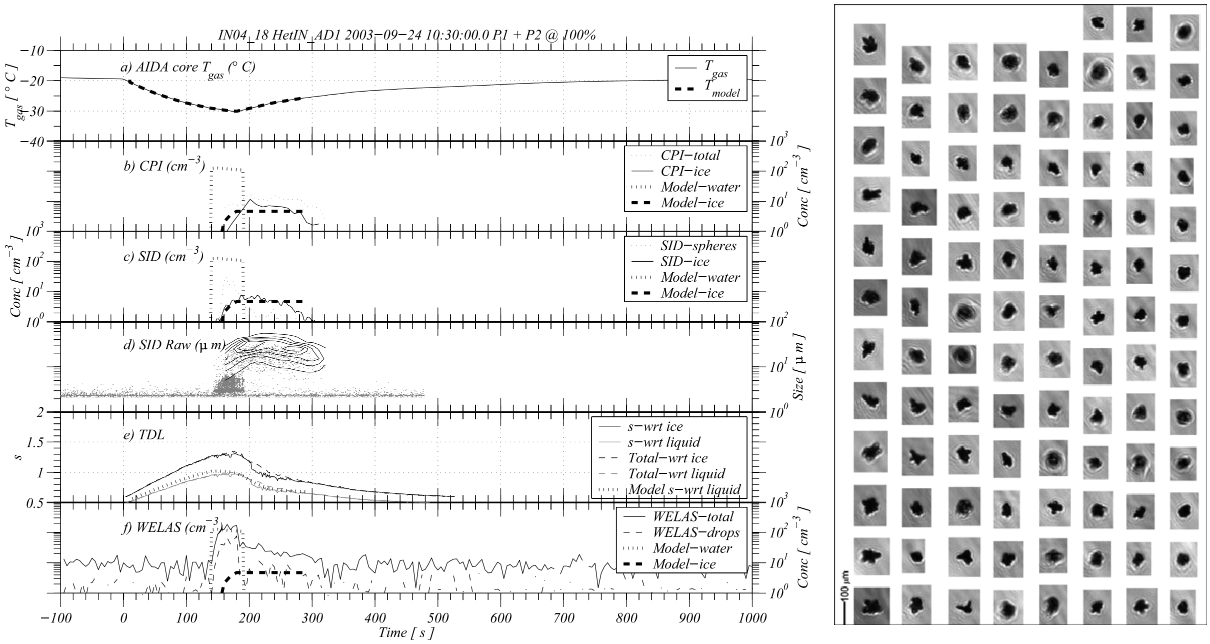

Fig. 9. Experiment IN04_18 showing ice nucleation on AD1 at −26°C. Plot captions are as for Fig. 6.

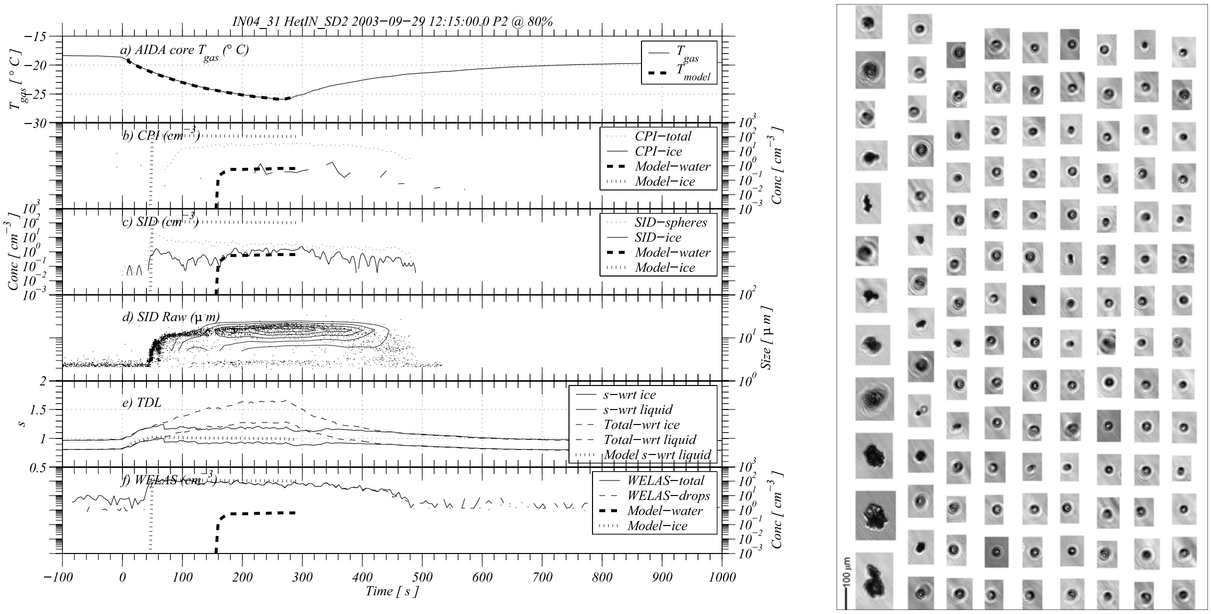

Fig. 10. Experiment IN04_31 showing ice nucleation on SD2 at −25°C. Plot captions are as for Fig. 6.

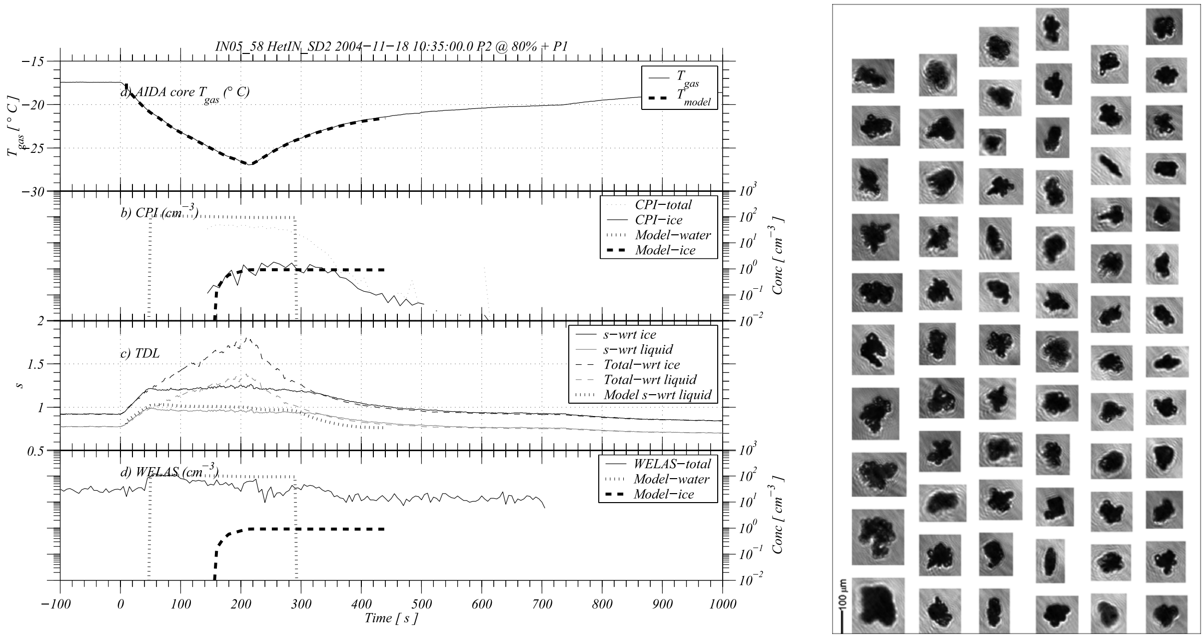

Fig. 11. Experiment IN05_58 showing freezing on SD2 at −26°C. Plot captions are as for Fig. 8.

Figure 12 shows an ESEM image of a typical ATD sample[5]. The particles are characterized by relatively uniform smooth faceted ensembles with strong fracture lines possibly the result of mechanical deformation. Full frame EDX analysis of this image confirmed the composition to be predominantly Si. This was typical of the composition of many of the larger ($D_p > 1\,\mu$m) particles observed. However, the morphology of the ATD could occasionally be highly varied presenting both smooth faceted, e.g. the target particle labelled "c" in Fig. 12, as well as granular or "shocked"-like appearances (target particle labelled "l"). Particles marked "a", "e" and "l" (selected as being representative of particle

---

[5] Reference: ATD0801

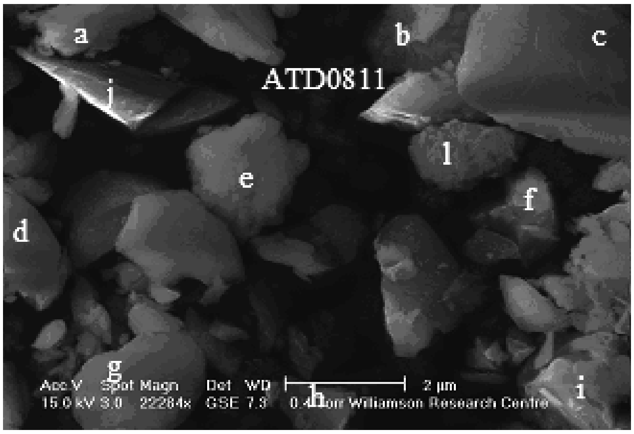

Fig. 12. ATD ESEM image (Sample ATD0811) showing both granular (or shocked, e.g. "l") and smooth faceted morphologies. Particles labelled "a" to "l" represent selected locations for EDX spot elemental analysis (scale 2 µm).

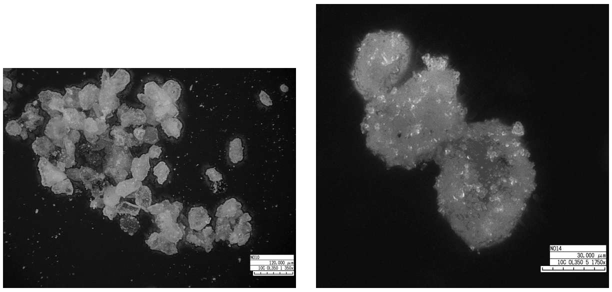

(a) Optical microscope image for scale equal to 120μm

(b) Optical microscope image for scale equal to 30μm

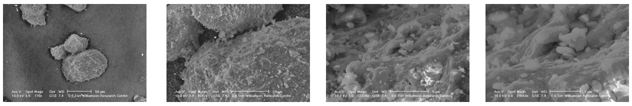

Fig. 13. Optical and scanning electron microscope images of SD2.

sizes in the range $1<D_p<2$ µm) in Fig. 12 revealed significant Ca loadings compared to the large particles. The reason for this is unclear. Table 5 shows the elemental summary of the EDX analysis by atomic percentage of the main elements.

Figure 13a and b are optical microscope images taken of the raw dust samples, showing the slightly rounded appearance of the primary "sand" granules, much larger than would have been passed by the chamber pre-filter system. These large particles are loosely coated with aggregates of much smaller granular particles some of which have been dislodged from the surface in the image. Figure 13c–f shows the corresponding ESEM images at increasing magnifications highlighting the sub 2 µm and coarse mode distributions. EDX for SD2 is summarized in Table 6.

Table 5. Atomic elemental percentages as determined by EDX spot analysis of particles "a" to "l" in Fig. 12a.

SAMPLE ATD Target	Atomic %	
Element	mean	σ
C	71.65	13.95
O	19.94	11.61
Mg	0.42	0.74
Al	0.66	0.50
Si	5.98	3.28
S	0.07	0.06
K	1.10	1.61
Ca	0.85	1.64
Fe	0.23	0.51

Table 6. Mean elemental atomic % composition of SD2 samples SD8030 and SD8032 based on multiple target EDX spot analyses. σ is the standard deviation of the sample.

SAMPLE SD2 Target	Atomic %	
Element	mean	σ
C	78.44	11.00
O	17.35	9.58
Mg	0.11	0.10
Al	0.73	0.65
Cl	0.04	0.06
Si	1.99	0.94
S	0.03	0.03
P	0.01	0.01
Ni	0.03	0.04
K	0.08	0.14
Ca	1.13	1.42
Fe	0.07	0.08

4.5 Other interesting experiments

Experiments IN02_77, 78, 80 and 81 were experiments on ATD where deposition nucleation was the mode of ice formation at $T=-25$°C (see Table 4). These experiments had no liquid water present throughout the run and yielded very different ice crystal habits to those observed in the freezing experiments and other deposition experiments at −33°C (IN02_72, IN02_73).

The ice crystal habits observed during these experiments were not consistent with those seen by Bailey and Hallett (2004) at −25°C, which were mostly plates and plate-like poly-crystals including overlapping parallel plates, side-planes, and spear heads. in fact they were actually a combination of needle-like crystals, T shaped crystals and perhaps

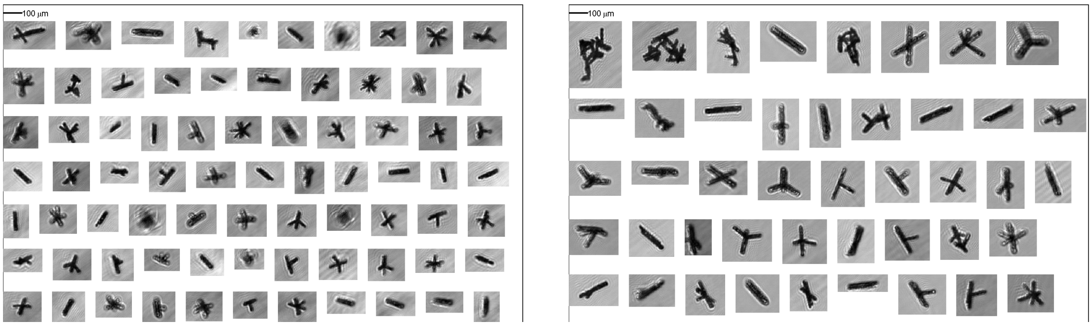

(a) (b)

Fig. 14. Ice crystal habits observed at −25°C for deposition nucleation on ATD. **(a)** shows experiment IN02_77 and **(b)** shows experiment IN02_78.

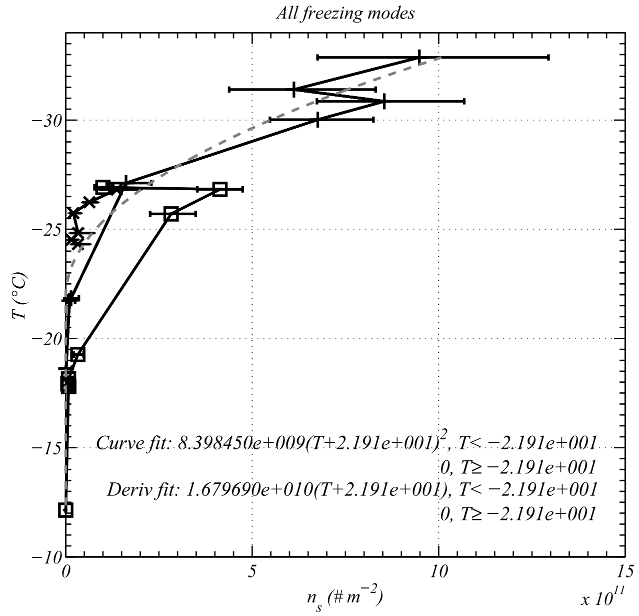

Fig. 15. This figure shows all of the fits for the three different dusts

rosette-like habits. Some aggregation was observed and could have been enhanced due to interlocking of the crystal shapes. The crystals observed during IN02_77 and 78 are shown in Fig. 14a and b, respectively.

To the authors' knowledge, this is the first time crystals of this habit have been observed to form at −25°C. Some of these crystals have appearances of sheaths, needles and rosettes that Bailey and Hallett (2004) observed at temperatures of −40, −50, −60 and −70°C.

The largest crystals in these sets of experiments were observed in experiments IN02_77 and IN02_78 and smaller, but similar examples of these crystals were observed in experiments IN02_80 and 81. More work is needed to test the exact range of conditions that produce these interesting crystals at −25°C. They seem to be formed by deposition nucleation on ATD at temperatures of around −25°C.

5 Discussion

The polynomial curves (see Sect. 4) for describing the nucleation efficiency of AD1, ATD and SD2 may be used as parameterisations for ice formation rates within atmospheric models in the freezing mode. However it should be noted that for the SD2 experiments the range of observations with respect to temperature is quite small and therefore does not show the variability of IASSD with temperature. Figure 15 shows a summary of all three curves, with the fitted polynomial which may also be used for simulations of ice formation in clouds. However, the differences between the different samples are significant; as noted from the "error" bars.

Sassen et al. (2003) noted an Ac cloud in the Florida region during CRYSTAL-FACE that was glaciated at temperatures between −5 and −8°C. This observation was coincident with a large amount of dust being advected by long range transport into the Florida region from the Sahara desert. The observation does not agree with the freezing parameterization in Fig. 4b, which showed that the IASSD was negligible in this temperature regime. Aircraft measurements with a continuous-flow diffusion chamber (CFDC) showed IN concentrations to be very large within the dust layer at heights corresponding to between −5 and −8°C (see DeMott et al., 2003); however, it should be noted that in this case the processing conditions of the IN chamber were much colder than the ambient conditions (about −36.5°C).

In addition to this there is also the possibility that the dust aerosols become more efficient as IN as they undergo processing in the atmosphere when they are blown across the Atlantic Ocean. Ansmann et al. (2008) have hinted that a possible reason for the discrepancy between their measurements and the results of DeMott et al. (2003); Sassen et al. (2003) was that

> "when the desert dust was advected over the ocean it could have been mixed with maritime particles and may have been influenced by anthropogenic pollution".

It has been shown by Krueger et al. (2004) that certain Ca containing compounds such as calcite and dolomite may react with nitric acid in the atmosphere to form nitrate salts; hence potentially modifying the chemical and physical properties of the dust. However, one might expect that the nitrate salts would reduce the IN activity. Another process that may be important to increasing the IN activity is chemical aging due to oxidation of the mineral surface by ozone. More work is needed to understand the impacts of such chemical aging processes on the dusts ability to act as an IN.

Other possible reasons for this could be that the dust sample we collected is not representative of all Sahara dust. Indeed the large particles in the sample are sifted out before introduction into the AIDA chamber in our experiments and there have been suggestions that large particles may have a higher IASSD, as noted by the size dependent nucleation rates measured by Archuleta et al. (2005) for aluminium oxide (Al_2O_3), alumina-silicate ($3Al_2O_3$:$2SiO_2$), and iron oxide (Fe_2O_3) particles. However, the EDX analysis for the the SD2 sample is in reasonable agreement with the values measured from aircraft samples (see McConnell et al., 2008; Krueger et al., 2004; Formenti et al., 2003) in terms of the Al:Si (0.37), Mg:Si (0.06) and Ca:Si (0.57) ratios. The main difference between the ATD sample and the SD2 sample was the Si content with ATD having around 4 times more Si by mol.

6 Conclusions

This has been a study of ice nucleation by three different dust samples in the temperature regime 0°C to −33°C. It was found that at temperatures warmer than −12°C, freezing on AD1, SD2 and ATD dusts was below our instrument detection threshold – which typically equates to less than 0.01% of dust particles being active as IN. All three samples showed increasing freezing efficiency with decreasing temperature. Deposition nucleation was negligible for temperatures warmer than −12.5°C (not shown). In the experiments shown here all of the dust particles in the AIDA acted as CCN, leaving no interstitial dust particles that could act as deposition nuclei. In the atmosphere however, it is reasonable to assume that this would happen and significant deposition nucleation could take place before the formation of liquid drops.

For ATD, we noted that freezing never took place at temperatures warmer than −12.5°C and increased by an order of magnitude at temperatures of −27°C. ATD also had a very strong deposition mode that was observed at temperatures colder than −24°C. We could not quantify this over a wide range of conditions. A polynomial fitted to the IASSD for the freezing mode needed adjustment in the regime where there were few observations (−20°C to −26°C) to get good agreement with between modelled and experimental data.

For AD1, we find that freezing nucleation is negligible (less than 1%) at temperatures warmer than −20°C, while for temperatures between −29.5°C and −33°C the IASSD increases, doubling over the temperature range of 3.5°C. Some activity in the deposition ice nucleation mode was noted for temperatures colder than −16°C, this was not observable at −12°C and was not observed at −26°C; however, this was typically very low (less than 1%).

For SD2 we found an increase in freezing efficiency between −24°C and −27°C. No freezing was observed for temperatures warmer than −24°C at least detectable to instrumental accuracy.

The results from this paper are supported by a recent lidar study by Ansmann et al. (2008) that freezing on Sahara dust is not efficient for $T > -20$°C. However, numerous observations suggest there is little doubt that there are processes that result in ice particle formation at warmer temperatures in many cloud types (Hobbs and Rangno, 1985, 1990). Whether this is due to contact nucleation or some other, more efficient freezing IN that are abundant in the atmosphere is a question that needs further research to answer.

This study has brought up several questions that need to be addressed in order to reconcile ice crystal concentrations in atmospheric models.

1. If the Sahara dust sample we collected is representative of the Sahara dust observed in the Florida clouds, then what was responsible for the glaciation of the Ac observed by Sassen et al. (2003)?

2. To what extent does atmospheric processing or coatings by other material affect the freezing efficiency of these nuclei?

3. Can the largest coarse mode aerosols explain the glaciation of the Ac observed by Sassen et al. (2003)?

An additional question that we find intriguing is what caused the appearance of thin columnar ice habits at −25°C in the ATD deposition experiments? And are these habits observed in the atmosphere under any conditions?

Appendix A

Equations and description of parcel model

The ACPIM code is a bin microphysical code including aerosol thermodynamics following Topping et al. (2005a,b). Solid inclusions within the solution can be taken into account such as dust particles. The model includes descriptions of the important liquid and ice phase microphysical processes; activation of drops; ice nucleation; aggregation, coalescence and riming. For this study we have neglected collisions and coalescences between the different hydrometeor species since this was of negligible importance for the experiments.

In a closed parcel, the total water content remains a constant and can be partially converted between water vapour, liquid or ice. The temperature of the air is calculated by consideration of the 1st law of thermodynamics for a closed parcel:

$$\frac{dT}{dt}=\left(\frac{R_m}{P}\frac{dP}{dt}-\frac{L_v}{T}\frac{dr_v}{dt}+\frac{L_f}{T}\frac{dr_i}{dt}\right)\frac{P}{c_{pm}} \tag{A1}$$

where R_m is the gas constant for moist air, L_v is the latent heat of vapourisation, L_f is the latent heat of fusion, c_{pm} is the specific heat of moist, cloudy air, r_v is the vapour mixing ratio and r_i is the ice mixing ratio (actually the rate of change due to an internal phase change).

Also, the total water content within the parcel remains constant:

$$\frac{dr_v}{dt}+\frac{dr_l}{dt}+\frac{dr_i}{dt}=0 \tag{A2}$$

where r_l is the water vapour mixing ratio. The time derivatives for r_l and r_i are calculated from the drop growth equations for different size bins (for r_l, see Pruppacher and Klett, 1997) and the ice growth and nucleation equations for the different size bins (for r_i, see Pruppacher and Klett, 1997).

$$\frac{dD_j}{dt}=\frac{4D^*M_w}{D_jR\rho_j}\left[\frac{e}{T}-\frac{e_{eq}}{T_{p,j}}\right] \tag{A3a}$$

$$T_{p,j}=T+\frac{2L_v}{4\pi D_jk^*}\frac{dm_j}{dt} \tag{A3b}$$

$$\frac{dm_j}{dt}=\frac{dD_j}{dt}\frac{dm_j}{dD_j}\approx\frac{\pi}{2}\rho_jD_j^2\frac{dD_j}{dt} \tag{A3c}$$

where the subscript j refers to a size bin, D is the particle size, M_w is the molecular mass of water, R is the gas constant, ρ is the density of the solution, e is the water vapour pressure, e_{eq} is the equilibrium vapour pressure (calculated using Kohler theory, with parameters supplied by a thermodynamic model), T is the air temperature and T_p is the temperature of the particle. The equations above are solved iteratively using Broydens method.

A simpler equation is used for the growth rate of ice particles by vapour deposition, following the electrostatic analogy (see Pruppacher and Klett, 1997, page 547):

$$\frac{dm_{\mathrm{ice},j}}{dt}=\frac{4\pi C_js_{v,i}}{\frac{RT}{e_{\mathrm{sat},i}(T)D^*M_w}+\frac{L_s}{k^*T}\left(\frac{L_sM_w}{RT}-1\right)} \tag{A4}$$

where L_s is the latent heat of sublimation, $s_{v,i}$ is the supersaturation with respect to ice, $e_{\mathrm{sat},i}(T)$ is the saturation vapour pressure over an ice surface, $m_{\mathrm{ice},j}$ is the mass of the jth ice bin and C_j is the capacitance factor. The derivatives are integrated using the DLSODAR numerical integrator available from netlib.

In the AIDA the chamber wall is an additional source of heat and moisture to the air inside. The reduction in pressure causes the air temperature to initially fall almost adiabatically, but the chamber wall temperature stays relatively constant. There is therefore a heat flux into the gas from the chamber wall, which increases as the temperature difference between the wall and the gas increases. The fact that the wall resides at a warmer temperature than the gas means the frost layer on the wall will tend to dry, acting as a vapour source to the gas inside the chamber.

We could attempt to model these complexities, but that is not the focus of this paper. Instead we have chosen to use measured T, P and total water mixing ratio to drive the ACPIM model. The time series of the measured T, P and total water mixing ratio, r_t were used to calculate time derivatives by fitting parabolas to the data over 10 s worth of data and differentiating this function analytically. This removes instrumental noise from the data, which would otherwise cause problems with the numerical ordinary differential equation (ODE) solver. These derivatives are used directly for the calculation of T and P in the model rather than using the above equation. The absolute starting value of the total water measurement was adjusted by a small amount so that in the model, liquid water condensed at the same time as in the observations.

For total water, r_t, the above equation is modified to take the additional flux in to account:

$$\frac{dr_v}{dt}+\frac{dr_l}{dt}+\frac{dr_i}{dt}=\frac{dr_{t,\mathrm{meas}}}{dt} \tag{A5}$$

where $r_{t,\mathrm{meas}}$ is the measured total water. In the model this is achieved by adjusting the water vapour derivative, r_v so that the above equation is satisfied.

Acknowledgements. Skillful support by the AIDA team is gratefully acknowledged. We thank L. Schütz from the University Mainz, Germany, for providing the AD1 sample, and Khaled Megahed for collecting the SD2 sample. We would like to acknowledge funding from Atmospheric Composition Change the European NeTwork of excellence (ACCENT). The CPI was provided through the University Facility of Atmospheric Measurement (UFAM) infrastructure and the SID probe is the property of the University of Hertfordshire. The first author would like to acknowledge J. Hallett and M. Bailey for interesting discussions on ice crystal habit growth. Additional support from the NERC APPRAISE-CLOUDS consortium is gratefully acknowledged (grant reference number NE/E01125X/1).

Edited by: D. Cziczo

References

Ansmann, A., Tesche, M., Althausen, D., Müller, D., Seifert, P., Freudenthaler, V., Heese, B., Wiegner, M., Pisani, G., Knippertz, P., and Dubovik, O.: Influence of Saharan dust on cloud glaciation in southern Morocco during the Saharan Mineral Dust Experiment, J. Geophys. Res., 113, D04210, doi:10.1029/2007JD008785, 2008.

Archuleta, C. M., DeMott, P. J., and Kreidenweis, S. M.: Ice nucleation by surrogates for atmospheric mineral dust and mineral dust/sulfate particles at cirrus temperatures, Atmos. Chem. Phys., 5, 2617–2634, 2005, http://www.atmos-chem-phys.net/5/2617/2005/.

Bailey, M. and Hallett, J.: Nucleation effects on the habit of vapour grown ice crystals from −18 to −42 °C, Q. J. Roy. Meteor. Soc., 128, 1461–1483, 2002.

Bailey, M. and Hallett, J.: Growth rates and habits of ice crystals between −20°C and −70°C, J. Atmos. Sci., 61, 514–544, 2004.

Connolly, P. J., Flynn, M. J., Ulanowski, Z., Ibbottson, T., Gallagher, M. W., and Choularton, T. W.: Calibration of the cloud particle imager probes using calibration beads and ice crystal analogs: the depth-of-field, J. Atmos. Ocean. Technol., 24, 1860–1879, 2007.

DeMott, P. J., Sassen, K., Poellot, M. R., Baumgardner, D., Rodgers, D. C., Brooks, S. D., Prenni, A. J., and Kreidenweis, S. M.: African dust aerosols as atmospheric ice nuclei, Geophys. Res. Lett., 30, 1732–1735, 2003.

Field, P. R., Möhler, O., Connolly, P., Krämer, M., Cotton, R., Heymsfield, A. J., Saathoff, H., and Schnaiter, M.: Some ice nucleation characteristics of Asian and Saharan desert dust, Atmos. Chem. Phys., 6, 2991–3006, 2006

Formenti, P., Elbert, W., Maenhaut, W., Haywood, J., and Andreae, M.: Chemical composition of mineral dust aerosol during the Saharan Dust Experiment (SHADE) airborne campaign in the Cape Verde region, September 2000, J. Geophys. Res., 108 (D18), 8576, doi:10.1029/2002JD002648, 2003.

Hirst, E., Kaye, P. H., Greenaway, R. S., Field, P. R., and Johnson, D.: Discrimination of micrometer-sized ice and supercooled droplets in mixed-phase cloud, Atmos. Environ., 35, 33–47, 2001.

Hobbs, P. V. and Rangno, A. L.: Ice particle concentrations in clouds, J. Atmos. Sci., 42, 2523–2549, 1985.

Hobbs, P. V. and Rangno, A. L.: Rapid development of high ice particle concentrations in small polar maritime cumuliform clouds, J. Atmos. Sci., 47, 2710–2722, 1990.

Krueger, B. J., Grassian, V. H., Cowib, J. P., and Laskin, A.: Heterogeneous chemistry of individual mineral dust particles from different dust source regions: the importance of particle mineralogy, Atmos. Environ., 38, 6253–6261, 2004.

Lawson, P., Baker, B. A., Schmitt, C. G., and Jensen, T. L.: An overview of microphysical properties of Artic clouds observed in May and July 1998 during FIRE ACE, J. Geophys. Res., 106, 14989–15014, 2001.

Linke, C., Möhler, O., Veres, A., Mohácsi, Á., Bozóki, Z., Szabó, G., and Schnaiter, M.: Optical properties and mineralogical composition of different Saharan mineral dust samples: a laboratory study, Atmos. Chem. Phys., 6, 3315–3323, 2006, http://www.atmos-chem-phys.net/6/3315/2006/.

Marcolli, C., Gedamke, S., Peter, T. and Zobrist, B.: Efficiency of immersion mode ice nucleation on surrogates of mineral dust, Atmos. Chem. Phys., 7, 5081–5091, 2007, http://www.atmos-chem-phys.net/7/5081/2007/.

McConnell, C. L., Highwood, E. J., Coe, H., Formenti, P., Anderson, B., Osborne, S., Nava, S., Desboeufs, K., Chen, G., and Harrison, M. A. J.: Seasonal variations of the physical and optical characteristics of Saharan dust: Results from the Dust Outflow and Deposition to the Ocean (DODO) experiment, J. Geophys. Res., 113, D14S05, doi:10.1029/2007JD009606, 2008.

Möhler, O., Wagner, R., Linke, C., Schnaiter, M., Saathoff, H., Mangold, A., Krämer, M., Ebert, V., Schutz, L., Field, P. R., Connolly, P. J., and Heymsfield, A. J.: Formation, growth and habit of ice crystals nucleated on mineral dust aerosol, 14th ICCP, Bologna, Italy, 2004.

Möhler, O., Field, P. R., Connolly, P., Benz, S., Saathoff, H., Schnaiter, M., Wagner, R., Cotton, R., Krämer, M., Mangold, A., and Heymsfield, A. J.: Efficiency of the deposition mode ice nucleation on mineral dust particles, Atmos. Chem. Phys., 6, 3007–3021, 2006, http://www.atmos-chem-phys.net/6/3007/2006/.

Murphy, D. M. and Koop, T.: Review of the vapour pressures of ice and supercooled water for atmospheric applications, Q. J. Roy. Meteor. Soc., 131, 1539–1565, 2005.

Pruppacher, H. R. and Klett, J. D.: Microphysics of clouds and precipitation, "Kluwer Academic Press", Norwell, 1997.

Sassen, K., DeMott, P. J., Prospero, J. M., and Poellot, M. R.: Saharan dust storms and indirect aerosol effects on clouds: CRYSTAL-FACE results, Geophys. Res. Lett., 30, 1633–1636, 2003.

Topping, D. O., McFiggans, G. B., and Coe, H.: A curved multicomponent aerosol hygroscopicity model framework: Part 1 – Inorganic compounds, Atmos. Chem. Phys., 5, 1205–1222, 2005a, http://www.atmos-chem-phys.net/5/1205/2005/.

Topping, D. O., McFiggans, G. B., and Coe, H.: A curved multicomponent aerosol hygroscopicity model framework: Part 2 – Including organic compounds, Atmos. Chem. Phys., 5, 1223–1242, 2005b, http://www.atmos-chem-phys.net/5/1223/2005/.

Vali, G.: Quantitative evaluation of experimental results on the heterogeneous freezing nucleation of supercooled liquids, J. Atmos. Sci., 28, 402–409, 1971.

Vali, G.: Freezing rate due to heterogeneous nucleation, J. Atmos. Sci., 31, 1843–1856, 1994.

Vali, G.: Repeatability and randomness in heterogeneous freezing nucleation, Atmos. Chem. Phys., 8, 5017–5031, 2008, http://www.atmos-chem-phys.net/8/5017/2008/.

Zimmermann, F., Weinbruch, S., Schütz, L., Hofmann, H., Ebert, M., Kandler, K. and Worringen, A.: Ice nucleation properties of the most abundant mineral dust phases, J. Geophys. Res., 113 (D23204), 8576, doi:10.1029/2008JD010655, 2008.